IGARSS 2024 - 2024 IEEE International Geoscience and Remote Sensing Symposium | 979-8-3503-6032-5/24/$31.00 ©2024 IEEE | DOI: 10.1109/IGARSS53475.2024.10641818

MONITORING LANDSLIDES ALONG THE JINSHA RIVER BASIN BASED ON DEMPSTER-SHAFER EVIDENCE THEORY WITH MULTI-SOURCE INSAR TIME SERIES

Qingyue Yang[1,2], *Zhang Yunjun*[1,2*], *Yidi Wang*[1,2], *Yosuke Aoki*[3], *Robert Wang*[1,2]

[1] National Key Laboratory of Microwave Imaging Technology, Aerospace Information Research Institute, Chinese Academy of Sciences, Beijing, China
[2] School of Electronics, Electrical and Communication Engineering, University of Chinese Academy of Sciences, Beijing, China
[3] Earthquake Research Institute, University of Tokyo, Tokyo, Japan

ABSTRACT

Synthetic aperture radar Interferometry (InSAR) has proven to be an effective landslide monitoring technique, especially for very slow landslides without observable morphological features. Integration of multi-source InSAR observations from different satellites/tracks could help reduce omissions and misjudgements of potential landslides, showing a promising trend toward automatic landslide detection and monitoring at regional or national scale. However, existing methods present poor error suppression performance, and are not capable of describing and solving potential information conflicts, due to the neglect of observation uncertainties during the integration. Here we propose a new integrated method based on Dempster-Shafer evidence theory to address these deficiencies. The two key steps are multi-source InSAR integration based on DST and a two-step decision rule. We apply the proposed method to the entire Jinsha River Basin using both ascending and descending Sentinel-1 SAR data from 2014 to 2023. The preliminary result on the Luoshui-Baini section based on two sources (ascending and descending orbits) identified 68 landslides, which is nearly the same between our method and the existing mosaic method.

Index Terms— Landslide, early detection, multi-source InSAR integrated decision, Dempster-Shafer evidence theory (DST)

1. INTRODUCTION

For regional landslide early detection, InSAR presents unique advantages due to large coverage, dense measurements, and relatively high sensitivity. However, single-track InSAR measurements have considerable uncertainties [1], which are mainly derived from various non-random noises (such as decorrelation noise from vegetation) and differences in measurement sensitivity and observability (shadow and layover) caused by systematic factors and terrain. Such uncertainties can subsequently lead to omissions or misjudgments of landslides. Integrated usage of multi-source observations from different satellites/tracks is expected to reduce possible omissions or misjudgments.

Integrated approach using multi-source InSAR at regional scale with automatic decision-making is desired to reduce labor costs. Existing methods are mainly belong to the mosaic method [2, 3, 4], which sets multiple thresholds (deformation, slope, aspect, and so on) to detect landslide candidates in each InSAR result and then directly mosaics all candidates. One major issue is that their successful applications highly depend on reliable thresholds, most of which are non-adaptive and based on prior knowledge or subjective experiences of experts. The implied assumption within these methods is that InSAR measurements are approximately accurate with only slight random errors. However, single-track InSAR measurements have considerable uncertainties. Some highly error-causing factors are prone to result in information conflicts among InSAR results, especially for big-data analysis at regional scale. In summary, since the potential uncertainties are neglected, the multi-source InSAR integrated decision based on existing methods present two deficiencies: a) poor error suppression performances, and more importantly, b) inability to describe and solve potential information conflicts.

In this paper, we propose a new method for multi-source InSAR integrated decision based on Dempster-Shafer evidence theory [5, 6], named MIID-DST, which is aimed to solve the deficiencies due to the ignorance of uncertainties more properly. First, MIID-DST takes full advantage of evidence (following the terminology used in DST, information is hereafter referred to as evidence) relevance and, to a certain extent, weakens the influence of bad evidence through reasoning and crosschecking, thereby forming enhanced error suppression in integration. Second, MIID-DST is capable of quantitatively describing evidence conflicts, providing integrated results with richer information, including pessimistic and optimistic estimations of deformation and an uncertain degree of estimation. In addition, the two states of weak deformation and artifacts, which are usually confused in exist-

ing methods, could be automatically distinguished, reducing the possibility of misjudgements.

2. METHODOLOGY

The workflow consists of three steps, as shown in Fig. 1.

Step 1: Single-track InSAR processing. Since the deformation rate is the most direct indicator for active landslides, single-track InSAR processing is required to convert the SAR data stacks to deformation rate maps. The related processing and details are described in Section 2.1.

Step 2: multi-source InSAR integration based on DST. The core contents is described in Section 2.2, consisting of a) the construction of the evidence reasoning model and b) a combination rule for InSAR observations. The integrated result can provide richer information than the existing methods, including the pessimistic estimation $Bel(Def.)$ and optimistic estimation $Pl(Def.)$ of deformation and the uncertainty degree of estimation $Und(Def.)$.

Step 3: Two-step decision rule. Based on the outputs of step 2, a two-step decision rule is designed in Section 2.3 to automatically detect suspected landslides in combination with morphological correction.

Finally, for the automatically detected landslide candidates, we manually eliminate potential misjudgements based on geological, morphological features (e.g., scarps, sliding masses, and bulging toes), and field investigations.

2.1. Single-track InSAR Processing

For each track of SAR images, we derive the surface displacement history in the radar line-of-sight (LOS) direction using InSAR time series analysis. More specificially, we use the topsStack processor [7] within the ISCE-2 software [8] for the interferogram stack processing and the MintPy software [9] for the InSAR time series analysis using the small baseline approach. Decorrelation noise is reduced using strategies such as small baseline combination [10], phase filtering, and multi-looking, tropospheric delays are corrected using ERA5 [11], and topographic residuals are corrected according to their relation to the perpendicular baseline (combined with deformation model) [12]. The remaining phase errors are neglected due to precise orbit of the Sentinel-1 satellite [13], short wavelength [14] and the long time coverage of the data used.

2.2. multi-source InSAR Integration Based on DST

2.2.1. Evidence Reasoning Model

We first construct the evidence reasoning model using its two most basic elements: the frame of discernment and mass function. In this study, the frame of discernment U is set as:

$$U = \{Def., Sta.\} \tag{1}$$

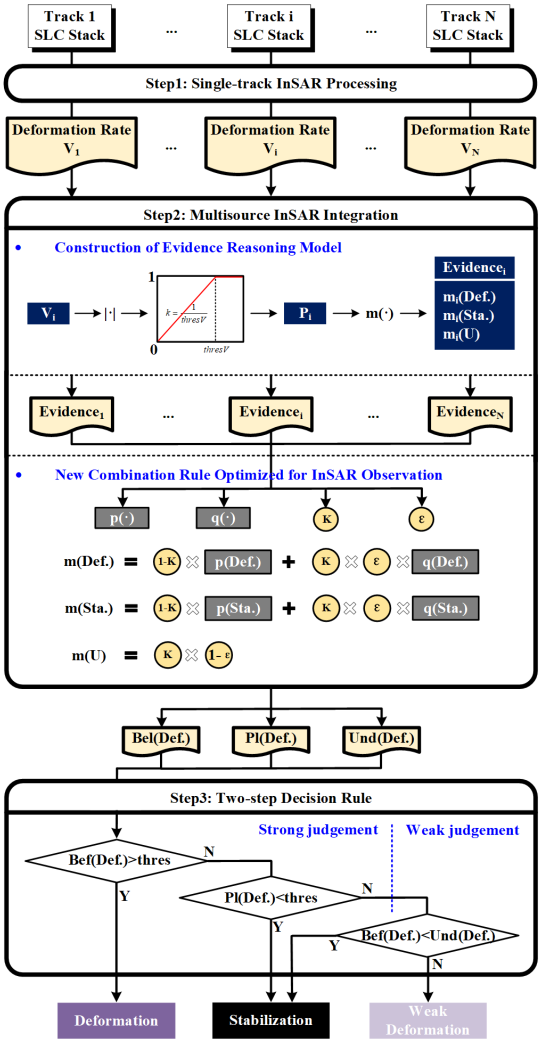

Fig. 1. The whole workflow of the proposed MIID-DST methodology.

where $Def.$ is the abbreviation for deformation, $Sta.$ is the abbreviation for stabilization.

The mass function $m(.)$ is defined as basic probability assignment function. In this study, the mass function, which relates the single-track InSAR deformation rate, is designed following the workflow illustrated in Fig. 1. First, a mapping function is constructed to transform the deformation rate V_i of the i^{th} single-track InSAR result into the deformation probability P_i, as:

$$P_i = \begin{cases} |V_i|/thresV\ , & |V_i| \le thresV \\ 1, & |V_i| > thresV \end{cases} \tag{2}$$

where $|.|$ is used to calculate the absolute value, $thresV$ is an empirical threshold of deformation to characterize the deformation rate of a certain landslide, which is highly dependent on the global accuracy σ of InSAR measurements, for instance, $thresV = 5\sigma$ in our case. Note that in order to avoid unrealistic amplification of phase noise, we do not calculate

and employ the 3D deformation rate to obtain the deformation probability. Next, the mass function $m(.)$ is designed to assign basic probabilities to all hypothesis in U, which can be expressed as:

$$\begin{cases} m_i\left(Def.\right) = P_i \\ m_i\left(Sta.\right) = 1 - P_i \\ m_i\left(U\right) = 0. \end{cases} \tag{3}$$

Suppose there are N pieces of evidence provided by InSAR results from N tracks, the evidence reasoning model can be established based on the frame of discernment in (1) and the mass function in (3).

2.2.2. *Combination Rule*

Following DST, the combination rule for InSAR observation can be described as:

$$\begin{cases} m\left(A\right) = \left(1-K\right)p\left(A\right) + K\varepsilon q\left(A\right), A = Def.or Sta. \\ m\left(U\right) = K\left(1-\varepsilon\right) \end{cases} \tag{4}$$

where K indicates the degree of evidence conflict, $p(A)$ denotes commonly shared belief among evidence, ε is the compound confidence, $q(A)$ is the average evidence support term optimized for InSAR observation with weights taken as the observation sensitivities. All of the above variables follow Sun's rule [6], except for the weighting of $q(A)$.

Additional information can be derived from the integrated results based on DST: a) the pessimistic estimation $Bel(Def.)$; b) the optimistic estimation $Pl(Def.)$; and c) the uncertainty degree of estimation $Und(Def.)$. The former two reflect the lower and upper limits of the integrated deformation probability, respectively; while the latter is a quantification of evidence uncertainty. They can be simplified as:

$$\begin{cases} Bel\left(Def.\right) = \sum_{A \subseteq Def.} m\left(A\right) = m\left(Def.\right) \\ Pl\left(Def.\right) = \sum_{A \cap Def. \neq \phi} m\left(A\right) = m\left(Def.\right) + m\left(U\right) \\ Und\left(Def.\right) = Pl\left(Def.\right) - m\left(Def.\right) = m\left(U\right) \end{cases} \tag{5}$$

2.3. Two-step Decision Rule

After the integration, a two-step decision rule (Fig. 1), consisting of strong judgment followed by weak judgment, is applied. The strong judgment refers to the common method, i.e., sets a threshold $thres$ (generally 1σ) to the deformation rate to identify the points in deformation and stabilization. Then, for those unjudged points in confusing states, a weak judgment is performed by comparison between $Bel(Def.)$ and $Und(Def.)$. The weak judgment has the potential to distinguish between the two states: weak deformations, and artifacts caused by residual errors (identified as $Sta.$).

3. EXPERIMENTS

3.1. Study Area

The Jinsha River starts from the southeastern Tibet Plateau, flows through the northwestern Yunnan-Guizhou Plateau, and ends in the southwestern Sichuan Basin (orange line in Fig. 2). The length of the mainstream is approximately 2316 km, covering an area of approximately 500,000 km^2. Under rapid tectonic uplift and river erosion, canyon-type landforms with valley depths greater than 1000 m are highly developed, which is prone to landslides [15]. Additionally, more than 20 giant cascade hydropower stations are built along the river. Hydropower construction activities tend to accelerate the hazard process and further increase the risk of landslides. In this paper, we focus on the entire Jinsha River Basin, to detect active landslides using satellite radar data.

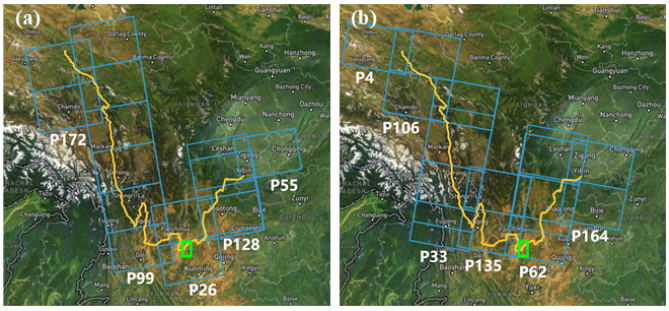

Fig. 2. Study area and dataset coverage. (a) The coverage of Ascending Sentinel-1 data in the study area. (b) The coverage of descending Sentinel-1 data in the study area. The green box show the areas demonstrated in Section 3.3.

3.2. Dataset

We use Sentinel-1 SAR data to derive a near-decadal surface deformation history covering the Jinshan River Basin from 2014 to 2023. 11 tracks with more than 6000 SAR images are used, including both ascending and descending orbits (blue boxes in Fig. 2). The Copernicus DEM with 1 arc second resolution is used for the topographic phase removal. Considering the complex terrain and relatively dense vegetation, we generate interferograms with the nearest 10 sequential connections, and with roughly one-year temporal baselines. Each interferogram is multilooked by 9 and 3 looks in the range and azmuth directions, respectively; and filtered by a Goldstein filtering with a strength of 0.8.

3.3. Preliminary Results

Here we present the preliminary landslide detection and monitoring results of the Luoshui-Baini section, a small area with known dense distribution of landslides (green box in Fig. 2).

Fig. 3 shows the deformation rate map and the displacement time series of some representative points. It is evident that the ascending and descending tracks have different measurement sensitivities to deformation and different noise levels, underlining the necessity of multi-source integration.

Fig. 4 shows the landslide detection result. The mosaic method is used for comparison, with a threshold value of 3

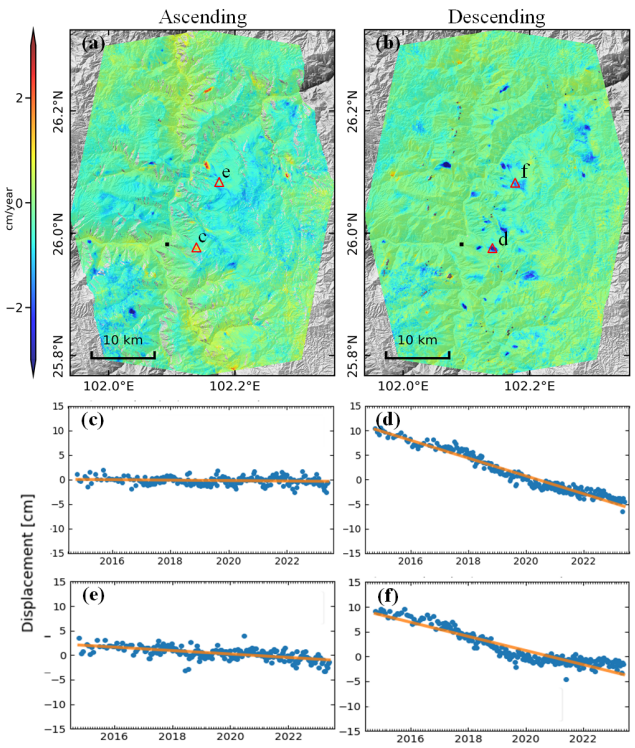

Fig. 3. Deformation rate maps and displacement time series. (a-b) are deformation rate maps derived from ascending and descending Sentinel-1 data, respectively. The location is marked by the green box in Fig. 2. (c-f) are displacement time series at point c-f in (a-b), respectively.

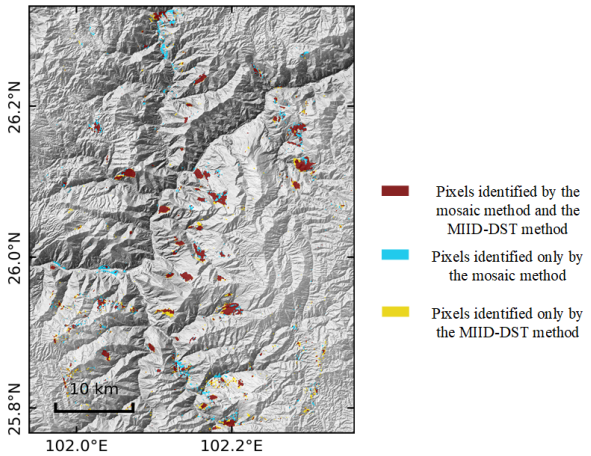

Fig. 4. Detected suspected landslides by the mosaic method with manually selected thresholds and the automatic MIID-DST method.

σ, which is manually adjusted according to the demonstration area. The mosaic method alone detected 23.97% of deformation pixels under the adopted threshold, MIID-DST alone detected 18.81% of deformation pixels, and both methods together detected 57.22% of the pixels. Overall, the pixels of landslides detected by both methods are highly consistent, partly due to the manually selected thresholds for the mosaic method and the limited evidence used for MIID-DST, which is only two. The pixels detected by the mosaic method only exhibit two distinct areas on the immediate sides of the river that show no obvious signs of deformation in the displacement time series, while the rest are irregularly distributed with no clear physical meaning. In total, our method detected about 68 landslides in the demonstrated region, encompassing landslides that have been sliding consistently for nearly a decade (Fig. 3(d)), as well as those that have ceased sliding in the last few years (Fig. 3(f)).

4. CONCLUSION

In this paper, we propose a novel method for multi-source InSAR integrated landslide detection based on the Dempster-Shafer evidence theory. The method could address the deficiencies of existing methods caused by ignorance of observation uncertainties. We applied the method to a decadal Sentinel-1 InSAR time series along a section of the Jinsha River. Expansion to the entire river basin and to incoporate ALOS-2 data is undergoing.

5. REFERENCES

[1] Liu X, Zhao C, Zhang Q, et al., "Integration of sentinel-1 and alos/palsar-2 sar datasets for mapping active landslides along the jinsha river corridor, china," *Engineering Geology*, vol. 284, pp. 106033, 2021.

[2] Zhao C, Lu Z, Zhang Q, et al., "Large-area landslide detection and monitoring with alos/palsar imagery data over northern california and southern oregon, usa," *Remote sensing of environment*, vol. 124, pp. 348–359, 2012.

[3] Bouali E H, Oommen T, and Escobar-Wolf R, "Mapping of slow landslides on the palos verdes peninsula using the california landslide inventory and persistent scatterer interferometry," *Landslides*, vol. 15, pp. 439–452, 2018.

[4] Xiaojie Liu, Chaoying Zhao, Yueping Yin, Roberto Tomás, Jing Zhang, Qin Zhang, Yunjie Wei, Meng Wang, and Juan M Lopez-Sanchez, "Refined insar method for mapping and classification of active landslides in a high mountain region: Deqin county, southern tibet plateau, china," *Remote Sensing of Environment*, vol. 304, pp. 114030, 2024.

[5] Shafer G, *A mathematical theory of evidence*, vol. 42, Princeton university press, 1976.

[6] Sun Q, Ye X, and Gu W, "A new combination rules of evidence theory," *ACTA ELECTONICA SINICA*, vol. 28, no. 8, pp. 117, 2000.

[7] Fattahi H, Agram P, and Simons M, "A network-based enhanced spectral diversity approach for tops time-series analysis," *IEEE Transactions on Geoscience and Remote Sensing*, vol. 55, no. 2, pp. 777–786, 2016.

[8] Rosen P A, Gurrola E, Sacco G F, et al., "The insar scientific computing environment," in *EUSAR 2012*. pp. 730–733, VDE.

[9] Yunjun Z, Fattahi H, and Amelung F, "Small baseline insar time series analysis: Unwrapping error correction and noise reduction," *Computers Geosciences*, vol. 133, pp. 104331, 2019.

[10] Paolo Berardino, Gianfranco Fornaro, Riccardo Lanari, and Eugenio Sansosti, "A new algorithm for surface deformation monitoring based on small baseline differential sar interferograms," *IEEE Transactions on geoscience and remote sensing*, vol. 40, no. 11, pp. 2375–2383, 2002.

[11] Hans Hersbach, Bill Bell, Paul Berrisford, Shoji Hirahara, András Horányi, Joaquín Muñoz-Sabater, Julien Nicolas, Carole Peubey, Raluca Radu, Dinand Schepers, et al., "The era5 global reanalysis," *Quarterly Journal of the Royal Meteorological Society*, vol. 146, no. 730, pp. 1999–2049, 2020.

[12] Heresh Fattahi and Falk Amelung, "Dem error correction in insar time series," *IEEE Transactions on Geoscience and Remote Sensing*, vol. 51, no. 7, pp. 4249–4259, 2013.

[13] Heresh Fattahi and Falk Amelung, "Insar uncertainty due to orbital errors," *Geophysical Journal International*, vol. 199, no. 1, pp. 549–560, 2014.

[14] Pius Kipng'etich Kirui, Eike Reinosch, Noorlaila Isya, Björn Riedel, and Markus Gerke, "Mitigation of atmospheric artefacts in multi temporal insar: a review," *PFG–Journal of Photogrammetry, Remote Sensing and Geoinformation Science*, vol. 89, pp. 251–272, 2021.

[15] Li D, Lu X X, Yang X, et al., "Sediment load responses to climate variation and cascade reservoirs in the yangtze river: A case study of the jinsha river," *Geomorphology*, vol. 322, pp. 41–52, 2018.